JOURNAL OF AIRCRAFT
Vol. 44, No. 5, September–October 2007

Autonomous Airborne Refueling of Unmanned Air Vehicles Using the Global Positioning System

Samer M. Khanafseh* and Boris Pervan†
Illinois Institute of Technology, Chicago, Illinois 60616

DOI: 10.2514/1.28195

Autonomous airborne refueling requires that the position of the receiving aircraft relative to the tanker be known very accurately and in real time. To meet this need, highly precise carrier-phase differential global positioning system solutions are being considered as the basis for navigation. However, the tanker introduces severe sky blockage into the autonomous airborne refueling mission, which reduces the number of visible global positioning system satellites and hence degrades the positioning accuracy. In this paper, we analyze the autonomous airborne refueling navigation problem in detail, define an optimal navigation architecture, and quantify navigation system availability. As part of this work, a high-fidelity dynamic sky-blockage model is developed and used to plan autonomous airborne refueling flight tests. The flight tests were conducted to obtain time-tagged global positioning system and attitude data that were processed offline to validate the blockage model.

I. Introduction

UNMANNED air vehicles (UAVs) have recently generated great interest because of their potential to perform hazardous missions without endangering the lives of pilots and crews. A UAV does not fatigue, and thus endurance is limited by mechanical constraints, weapon payload, and, primarily, fuel [1,2]. Therefore, aerial refueling is a key capability in making full use of the benefits inherent in the UAV [1,3]. Because UAVs are unmanned, such refueling missions must take place autonomously. Autonomous aerial refueling (AAR) is considered a technical challenge [2] and a relatively new area of research, with most of the previous work being done within the past five years.

A key role in successful refueling is to estimate the position of the UAV relative to the tanker very accurately and in real time. In addition, to ensure safety and operational usefulness, the navigation architecture must provide high levels of integrity, continuity, and availability. Integrity risk is the likelihood of an undetected navigation error or failure that results in hazardously misleading information. Continuity risk is the probability of a detected but unscheduled navigation function interruption after an operation has been initiated. Availability is the fraction of time the navigation function is considered usable (as determined by its agreement with the accuracy, integrity, and continuity requirements) before an operation is initiated. To meet these requirements, several instruments and methods for relative navigation have been pursued. Most of the previous research focused on passive and active vision sensors. Passive vision systems do not require the cooperation of the target in any way [4]. The disadvantages with passive systems come from their significant computational burden and sensitivity to lighting conditions. In contrast, active vision systems communicate and coordinate with the target using a set of structured light beacons and a sensor [5,6]. Although active vision sensors are more robust to lighting conditions, their tracking performance is highly sensitive to the beacon arrangement and measurement dropouts. A further drawback to vision systems in general is that additional equipment must be installed on the UAV (and on the tanker in the case of the active vision systems), which can be weight- and cost-inefficient.

The global position system (GPS) is a passive, satellite-based ranging system. The nominal GPS satellite constellation consists of 24 satellites (there are typically 27–31 operational satellites at any given time) in circular orbits. GPS satellites transmit the radio ranging signals and navigation data in two different frequencies: L1 (1575.42 MHz) and L2 (1227.60 MHz). The fundamental principle behind GPS satellite ranging is the measurement of the phase offset between the received code for a given satellite and an identical code generated internally in the receiver. A user can estimate his position by obtaining ranges to the GPS satellites in view [7].

Although GPS has been used in the past in aircraft landing [8] and aircraft-to-aircraft positioning [9], GPS was not originally considered a candidate for AAR terminal navigation because of AAR's stringent fault-free integrity and accuracy requirements and the severe sky blockage that the tanker causes to the GPS satellites. In this work, terminal navigation is used to mean the final-approach navigation of the UAV rendezvous with the tanker. Recently, however, algorithms using dual-frequency GPS carrier-phase have been developed to land aircraft on carrier ship decks with requirements similar to AAR [10,11]. A benefit of using GPS for AAR is that GPS systems will be installed anyway onboard the UAV for navigation during all other phases of flight; there are no weight or cost penalties in expanding its use. In this paper, we first introduce a proposed shipboard relative GPS (SRGPS) navigation architecture [10], which uses carrier-phase differential GPS (CPDGPS), and we exploit it as a preliminary basis for AAR navigation.

Two main types of in-flight refueling systems are currently in use: the *drogue* system that most U.S. Navy aircraft use and the *boom* system that the U.S. Air Force uses. In the drogue system, a hose with a cone-shaped basket at the end is winched out from the tanker wing (Fig. 1a). The receiving aircraft has a probe that the pilot guides into the basket. The boom system, in contrast, has a fixed boom that is lowered from the tanker end and is extended into a socket on the top of the receiving aircraft (Fig. 1b). Today, there are three types of tanker airplanes used for in-flight air refueling: KC-135, KC-10, and KC-130. If the KC-10 and KC-130 are used with the drogue system, the sky blockage caused by the tanker aircraft is relatively small because the drogue hose is winched from the wings of the airplane (Fig. 1a). Although KC-10 is larger than KC-135, there are only 59 KC-10s in American inventory compared with 615 KC-135 airplanes. In this work, the KC-135 and the boom system are studied in detail.

In this paper, we analyze the AAR navigation problem in detail, define an optimal navigation architecture, and quantify navigation system availability. To account for the obstruction that the tanker

Received 4 October 2006; accepted for publication 20 March 2007.

*Ph.D. Candidate, Mechanical, Materials and Aerospace Engineering Department, 10 West 32nd Street. Student Member AIAA.

†Associate Professor, Mechanical, Materials and Aerospace Engineering Department, 10 West 32nd Street. Senior Member AIAA.

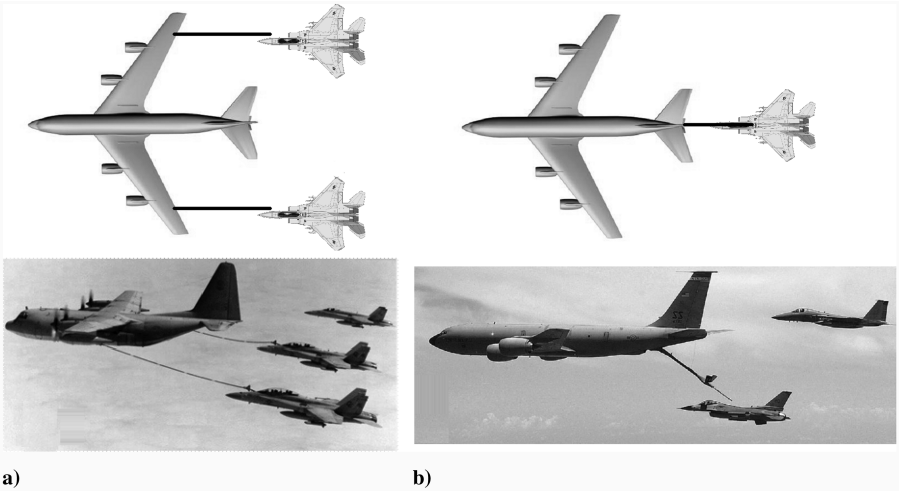

a) b)

Fig. 1 Air refueling systems: a) drogue system and b) boom system.

introduces to the GPS signal, a high-fidelity dynamic sky-blockage model is developed. The blockage model and the navigation algorithms are used to conduct availability sensitivity and global availability analyses. In addition, the analytical tools established throughout this work were used to plan AAR flight tests that took place in September 2004. The goals of these tests were to validate the AAR algorithms and the availability simulations. Time-tagged GPS and inertial navigation system (INS) data were collected to use with offline GPS algorithms and to verify the sky-blockage model and simulations. Validation is obtained by comparing the predicted-blocked satellites, as estimated using the dynamic model, with the actually blocked satellites, as indicated by measured drops in signal strength and phase-lock losses of the measurements. The results of these experimental trials are also presented in this paper.

II. Availability Analysis

A. Navigation Algorithm

AAR applications are equipped with dual-frequency (L1 and L2) GPS receivers because they have access to the military-encrypted L2 signal. The precision of code-phase measurements PR with nominal receiver thermal noise is typically 0.3–1 m (σ_{PR}) and less than 1 cm σ_ϕ for carrier-phase measurements ϕ. In addition to receiver thermal noise, a number of other ranging error sources exist such as clock biases τ, ionospheric I, tropospheric delays T, multipath, and all other additional biases d (such as interfrequency biases and antenna-phase-center variations), which limit standard civil GPS positioning accuracy to roughly the 10-m level [7]. The carrier measurement contains the measured fractional cycle and the integer number of cycles between the receiver and the satellite. However, when the receiver acquires the GPS signal, it has no information regarding the correct integer number of cycles. The unknown integer is called a cycle ambiguity N, and the process of its estimation is known as *cycle-ambiguity resolution*. The L1 and L2 code PR and carrier ϕ measurements can, for a given satellite i, be modeled as follows:

$$\phi_{L1}^{(i)} = \rho^{(i)} + \tau^{(i)} + \tau_{\mathrm{RCV}} + \lambda_{L1} N_{L1}^{(i)} - I^{(i)} + T^{(i)} + d_{L1}^{(i)} + \varepsilon_{\phi L1}^{(i)} \quad (1)$$

$$\phi_{L2}^{(i)} = \rho^{(i)} + \tau^{(i)} + \tau_{\mathrm{RCV}} + \lambda_{L2} N_{L2}^{(i)} - \frac{f_{L1}^2}{f_{L2}^2} I^{(i)} + T^{(i)} + d_{L2}^{(i)} + \varepsilon_{\phi L2}^{(i)} \quad (2)$$

$$\mathrm{PR}_{L1}^{(i)} = \rho^{(i)} + \tau^{(i)} + \tau_{\mathrm{RCV}} + I^{(i)} + T^{(i)} + d_{L1}^{(i)} + \varepsilon_{\mathrm{PR}L1}^{(i)} \quad (3)$$

$$\mathrm{PR}_{L2}^{(i)} = \rho^{(i)} + \tau^{(i)} + \tau_{\mathrm{RCV}} + \frac{f_{L1}^2}{f_{L2}^2} I^{(i)} + T^{(i)} + d_{L2}^{(i)} + \varepsilon_{\mathrm{PR}L2}^{(i)} \quad (4)$$

where $d_{L1}^{(i)}$ and $d_{L2}^{(i)}$ are the L1 and L2 additional biases (interfrequency and phase center) for a given satellite i; f_{L1} and f_{L2} are the L1 and L2 carrier signal frequencies; $I^{(i)}$ are the L1 ionospheric delay errors for a given satellite i; $N_{L1}^{(i)}$ and $N_{L2}^{(i)}$ are L1 and L2 cycle ambiguity for a given satellite i;$\mathrm{PR}_{L1}^{(i)}$ and $\mathrm{PR}_{L2}^{(i)}$ are the L1 and L2 pseudorange raw measurements for a given satellite i; $T^{(i)}$ are the tropospheric errors for a given satellite i; $\varepsilon_\phi^{(i)}$ and $\varepsilon_{\mathrm{PR}}^{(i)}$ are the carrier-phase and pseudorange remaining multipath and thermal noise errors; λ_{L1} and λ_{L2} are the L1 and L2 carrier signal wavelengths; $\rho^{(i)}$ is the range from the receiver to a given satellite i; $\tau^{(i)}$ and τ_{RCV} are the clock biases for the ith satellite and the receiver; and $\phi_{L1}^{(i)}$ and $\phi_{L2}^{(i)}$ are the L1 and L2 carrier-phase raw measurements for a given satellite i.

The realization of centimeter-level performance requires the correct resolution of carrier-phase cycle ambiguities for GPS satellites in view. The cycle-resolution problem is nontrivial in general. A number of methods have been used to obtain the resolution. Satellite motion can provide the observability for the estimation of the cycle ambiguities. Unfortunately, the rate of satellite motion is relatively slow in comparison with the timescales of the refueling mission. However, carrier measurements at the two frequencies can be combined to create a beat frequency measurement with wavelength λ_w of 86 cm, generally known as a *wide-lane observable* [7]. Because of the longer wavelength, the wide-lane cycle ambiguities are easier to identify using code-phase measurements. Once the wide-lane cycle ambiguities are identified, the wide-lane observable provides a reliable measurement source (more accurate than code phase) from which the cycle ambiguities for L1 or L2 can be resolved. In addition, dual-frequency approaches can be made more effective through the use of measurement filtering and satellite redundancy.

The AAR navigation algorithms provide robust CPDGPS performance by combining the complementary benefits of geometry-free filtering [12] and geometric redundancy [10,11]. Geometry-free, by definition, does not depend on the geometry of the satellites or the user location and eliminates most of the nuisance terms and errors. On the other hand, geometric redundancy is highly dependent on the satellite geometry and is very sensitive to decorrelation errors and the correlation between the measurements. A geometry-free measurement of the wide-lane cycle ambiguity N_w can be formed by subtracting the narrow-lane pseudorange PR_n (which reduces the PR errors compared with L1 or L2) from the wide-lane carrier ϕ_w (which eliminates the geometry-dependent term ρ and the nuisance terms τ, T, and I), as shown in Eqs. (5–7) [7,12]. However, other frequency-dependent biases d_w (such as interfrequency biases or antenna-phase-center variations) are not eliminated in the geometry-free calculation [Eq. (7)]. Assuming that d_w changes slowly with time (with respect to the filtering periods used later in this work), their filtered components will be eliminated in the double-difference

operation performed inside the service volume (more on this to come shortly). However, if the tanker and UAV antennas are different, phase-center variations can be calibrated such that any residual errors are included in the carrier-phase error model used.

$$\mathrm{PR}_n^{(i)} = \left(\frac{\mathrm{PR}_{L1}^{(i)}}{\lambda_{L1}} + \frac{\mathrm{PR}_{L2}^{(i)}}{\lambda_{L2}}\right)\left(\frac{\lambda_{L1}\lambda_{L2}}{\lambda_{L1}+\lambda_{L2}}\right) = \rho^{(i)} + \tau^{(i)} + \tau_{\mathrm{RCV}} + T^{(i)} + \frac{\lambda_{L2}}{\lambda_{L1}} I^{(i)} + d_{\mathrm{PR}n}^{(i)} + \left(\frac{\varepsilon_{L1}^{(i)}}{\lambda_{L1}} + \frac{\varepsilon_{L2}^{(i)}}{\lambda_{L2}}\right)\left(\frac{\lambda_{L1}\lambda_{L2}}{\lambda_{L1}+\lambda_{L2}}\right) \tag{5}$$

$$\phi_w^{(i)} = \left(\frac{\phi_{L1}^{(i)}}{\lambda_{L1}} - \frac{\phi_{L2}^{(i)}}{\lambda_{L2}}\right)\left(\frac{\lambda_{L1}\lambda_{L2}}{\lambda_{L2}-\lambda_{L1}}\right) = \rho^{(i)} + \tau^{(i)} + \tau_{\mathrm{RCV}} + T^{(i)} + \left(\frac{\lambda_{L1}\lambda_{L2}}{\lambda_{L2}-\lambda_{L1}}\right)\left(N_{L1}^{(i)} - N_{L2}^{(i)}\right) + \frac{\lambda_{L2}}{\lambda_{L1}} I^{(i)} + d_{\phi w}^{(i)} + \left(\frac{\varepsilon_{L1}^{(i)}}{\lambda_{L1}} - \frac{\varepsilon_{L2}^{(i)}}{\lambda_{L2}}\right)\left(\frac{\lambda_{L1}\lambda_{L2}}{\lambda_{L2}-\lambda_{L1}}\right) \tag{6}$$

$$\phi_w^{(i)} - \mathrm{PR}_n^{(i)} = \left(\frac{\lambda_{L1}\lambda_{L2}}{\lambda_{L2}-\lambda_{L1}}\right)\left(N_{L1}^{(i)} - N_{L2}^{(i)}\right) + d_w^{(i)} + \varepsilon_w^{(i)} = \lambda_w N_w^{(i)} + d_w^{(i)} + \varepsilon_w^{(i)} \tag{7}$$

where $\mathrm{PR}_n^{(i)}$ is the narrow-lane pseudorange for a given satellite i; $d_{\mathrm{PR}n}^{(i)}$ is the narrow-lane component of the biases, equal to

$$\frac{d_{L1}^{(i)}\lambda_2 + d_{L2}^{(i)}}{\lambda_{L1}+\lambda_{L2}}$$

$\phi_w^{(i)}$ is the wide-lane carrier phase for a given satellite i; $d_{\phi w}^{(i)}$ is the wide-lane component of the biases, equal to

$$\frac{d_{L1}^{(i)}\lambda_2 - d_{L2}^{(i)}}{\lambda_{L2}-\lambda_{L1}}$$

$N_w^{(i)}$ is the wide-lane cycle ambiguity for a given satellite i; λ_w is the wide-lane wavelength; $d_w^{(i)} = d_{\phi w}^{(i)} - d_{\mathrm{PR}n}^{(i)}$; and ε_w are remaining errors that are modeled as first-order Gauss–Markov, with autocorrelation time constant α and a variance σ_w^2 equal to

$$\sigma_w^2 = \left(\frac{\sigma_{\phi L1}^2}{\lambda_{L1}^2} + \frac{\sigma_{\phi L2}^2}{\lambda_{L2}^2}\right) + \left(\frac{\lambda_{L2}-\lambda_{L1}}{\lambda_{L1}+\lambda_{L2}}\right)^2\left(\frac{\sigma_{\mathrm{PR}L1}^2}{\lambda_{L1}^2} + \frac{\sigma_{\mathrm{PR}L2}^2}{\lambda_{L2}^2}\right)$$

where σ_w^2 is the wide-lane observable variance; $\sigma_{\phi L1}^2$ and $\sigma_{\phi L2}^2$ are the L1 and L2 carrier-phase noise variance; and $\sigma_{\mathrm{PR}L1}^2$ and $\sigma_{\mathrm{PR}L2}^2$ are the L1 and L2 pseudorange noise variance.

When the UAV is far from the tanker, inside or outside the service volume [i.e., the region in which the tanker reference GPS measurements are available to the UAV (Fig. 2a)], the wide-lane observable [left-hand side of Eq. (7)] is calculated and filtered. For each satellite i, the filtered wide-lane observable is calculated by averaging the wide-lane cycle ambiguities in Eq. (7) over a corresponding time interval $T^{(i)}$. The variance of the filtered wide-lane ambiguities, $\sigma_{\bar{N}w}^2$, is estimated using a first-order Gauss–Markov measurement error model to account for correlation, caused mainly by multipath, between measurements [10]:

$$\sigma_{\bar{N}w}^{(i)2} = \frac{2\sigma_w^{(i)2}}{T^{(i)}/\alpha} - \frac{2\sigma_w^{(i)2}}{(T^{(i)}/\alpha)^2}\left(1 - e^{-T^{(i)}/\alpha}\right) \tag{8}$$

where $T^{(i)}$ is the time interval over which the wide-lane cycle ambiguities for satellite i has been filtered, and α is the multipath autocorrelation time constant of ε_w.

Using the wide-lane observable is beneficial because long (geometry-free) filter durations can be used before the service volume entry. However, as Eq. (7) shows, ambiguity resolution is not possible outside the service volume because of errors such as antenna-phase-center variations and interfrequency biases, which can only be eliminated using double-differencing inside the data link range. The cycle-ambiguity resolution at the L1 and L2 wavelengths

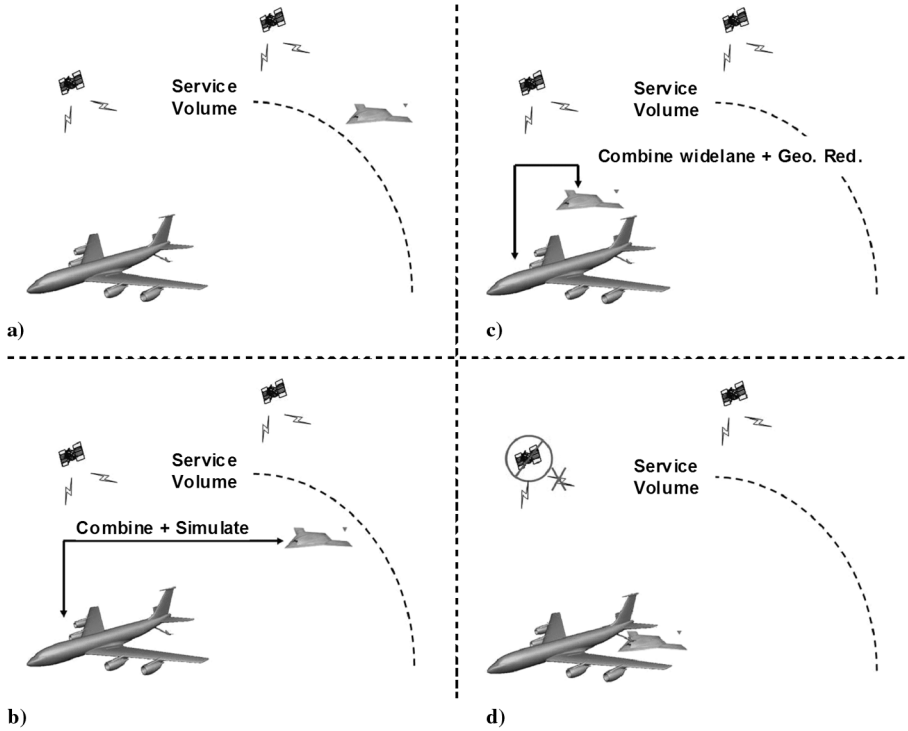

Fig. 2 Conceptual drawing shows the main steps in the refueling algorithm: a) both aircraft prefiltering wide-lane cycle ambiguities before the UAV enters the service volume, b) tanker combines filtered wide-lane integers to simulate the mission, c) geometric redundancy when the UAV is in the observation position, and d) some satellites will be blocked when the UAV goes below the tanker belly.

using geometric redundancy is also limited to the service volume. In this space, the UAV has access to the tanker reference carrier-phase measurements and filtered wide-lane observables and is more robust to ionospheric and tropospheric decorrelation, because the distance between the UAV and the tanker is small. Therefore, only when the UAV is near the tanker can carrier-phase geometric redundancy be used for cycle estimation of L1 and L2 integers. In addition, a double-difference operation $\nabla\Delta$ between the tanker and UAV measurements and between a preselected reference satellite measurement k is used to eliminate the additional biases from the filtered wide-lane observable d_w [Eq. (9)] and the satellite and receiver clock biases $\tau^{(i)}$ and τ_{RCV} from the carrier-phase measurements [Eqs. (10) and (11)]:

$$\nabla\Delta\bar{N}_w^{(i,k)} = \nabla\Delta N_{L1}^{(i,k)} - \nabla\Delta N_{L2}^{(i,k)} + \varepsilon_{\nabla\Delta\bar{N}w}^{(i,k)} \tag{9}$$

$$\nabla\Delta\phi_{L1}^{(i,k)} = -\Delta e^{(i,k)T}x + \lambda_{L1}\nabla\Delta N_{L1}^{(i,k)} + \varepsilon_{\nabla\Delta\phi L1}^{(i,k)} \tag{10}$$

$$\nabla\Delta\phi_{L2}^{(i,k)} = -\Delta e^{(i,k)T}x + \lambda_{L2}\nabla\Delta N_{L2}^{(i,k)} + \varepsilon_{\nabla\Delta\phi L2}^{(i,k)} \tag{11}$$

where x is the relative position vector between the UAV and the tanker; $\varepsilon_{\Delta\bar{N}w}$ are differenced and filtered errors, which are normally distributed with a variance of $\sigma^2_{\bar{N}w}$; $\Delta e^{(i,k)}$ is the difference in the line-of-sight vector between satellite i and satellite k; $\nabla\Delta$ is the double-difference operation between the tanker and the UAV and satellites i and k; and $\nabla\Delta\bar{N}_w$ is the double-difference filtered wide-lane cycle-ambiguity estimate.

Stacking Eqs. (9–11) in matrix form for all satellites, L1 and L2 integers can be estimated:

$$\begin{bmatrix} \nabla\boldsymbol{\Delta}\bar{\mathbf{N}}_w \\ \nabla\boldsymbol{\Delta}\boldsymbol{\varphi}_{L1} \\ \nabla\boldsymbol{\Delta}\boldsymbol{\varphi}_{L2} \end{bmatrix} = \begin{bmatrix} \mathbf{0} \\ -\boldsymbol{\Delta}\mathbf{e}^T \\ -\boldsymbol{\Delta}\mathbf{e}^T \end{bmatrix} \cdot x + \begin{bmatrix} \mathbf{I} & -\mathbf{I} \\ \lambda_{L1}\mathbf{I} & \mathbf{0} \\ \mathbf{0} & \lambda_{L2}\mathbf{I} \end{bmatrix} \begin{bmatrix} \nabla\boldsymbol{\Delta}\mathbf{N}_{L1} \\ \nabla\boldsymbol{\Delta}\mathbf{N}_{L2} \end{bmatrix} + \begin{bmatrix} \boldsymbol{\varepsilon}_{\nabla\Delta\varphi\bar{N}w} \\ \boldsymbol{\varepsilon}_{\nabla\Delta\varphi L1} \\ \boldsymbol{\varepsilon}_{\nabla\Delta\varphi L2} \end{bmatrix} \tag{12}$$

At this stage, integer fixing is facilitated using the least-squares ambiguity decorrelation adjustment (LAMBDA) bootstrap method [13] to meet the fault-free integrity requirements. The bootstrap rounding method fixes ambiguities sequentially and provides a measure of the probability of correct fix (PCF) throughout each step of the fixing process. Based on [14], the variance of the ith ambiguity, given that the previous integers in the set $\mathrm{I} = \{1, 2, \ldots, i-1\}$ are fixed ($\sigma_{i/I}$), is the i, i element of the diagonal matrix D resulting from LDL^T decomposition of the float-ambiguity estimate-covariance matrix (decorrelated float-ambiguity estimate covariance in the case of using LAMBDA). The probability that integers 1:k are fixed correctly, given that all integers in the set $\mathrm{I} = \{1, \ldots, k-1\}$ are fixed ($\mathrm{PCF}_{k/I}$) correctly, is given by

$$\mathrm{PCF}_{k|I} = \prod_{i=1}^{k} 2\Phi\left(\frac{1}{2\sigma_{i|I}}\right) - 1 \tag{13}$$

where $\mathrm{PCF}_{k/I}$ is the probability that integers 1:k are fixed correctly, given that all integers in the set $\mathrm{I} = \{1, \ldots, k-1\}$ are fixed correctly,

$$\Phi(x) = \int_{-\infty}^{x} \frac{1}{\sqrt{2\pi}} \exp(-1/2v^2)\, \mathrm{d}v$$

and $\sigma_{i/I}$ is the variance of the ith least-squares ambiguity, given that the previous integers in the set $\mathrm{I} = \{1, \ldots, i-1\}$ are fixed.

The fixing process is performed for those ambiguities that can be fixed with a PCF [Eq. (13)] that is higher than the predefined threshold. In this work, we assume that 10% of the fault-free integrity budget of 10^{-7} is allocated to the cycle resolution, which leads to a PCF threshold of $1–10^{-8}$. The remaining ambiguities remain floating. To maintain the fault-free integrity associated with ambiguity resolution, which is consumed by the PCF budget in the fixing step, the geometric redundancy (including fixing ambiguities) is performed only once.

The AAR mission is different from other missions because of the severe blockage that is introduced by the tanker. This blockage reduces the number of visible GPS satellites and hence degrades the positioning accuracy (Fig. 1). To predict, and hence limit, the effect of the satellite blockages, the AAR mission can be simulated using the known GPS constellation at the time of the mission, the heading of the tanker, and the blockage model (Fig. 2b). Once the UAV enters the service volume, the tanker has access to the UAV measurements and is able to simulate the AAR mission (using a covariance analysis similar to the one described in Sec. II.D) to decide whether to abort, continue, or modify the refueling path. If the positioning accuracy and fault-free integrity requirements are met based on the predictive simulation, the UAV will move to the observation position (tanker lead formation), in which the UAV is just off the wing of the tanker and in the clear sky (Fig. 2c). At that point, the carrier-phase geometric redundancy (including fixing ambiguities) can be safely exploited for cycle estimation of L1 and L2 integers. From this point forward, CPDGPS positioning can be implemented and the relative vector between the UAV and the tanker (x) is estimated using Eq. (14). Again, when the UAV moves to the contact position (below the belly of the tanker), some satellites will be blocked and removed from the fixed integer set (Fig. 2d) (remember that cycle-ambiguity estimation is only done once: at the geometric-redundancy step), but the positioning accuracy remains within the required limit because the predictive simulation has already taken these blockages into account:

$$\begin{aligned} \nabla\Delta\phi_{L1}^{(i,k)} - \lambda_{L1}\nabla\Delta N_{L1}^{(i,k)} &= -\Delta e^{(i,k)T}x + \varepsilon_{\nabla\Delta\phi L1}^{(i,k)} \\ \nabla\Delta\phi_{L2}^{(i,k)} - \lambda_{L2}\nabla\Delta N_{L2}^{(i,k)} &= -\Delta e^{(i,k)T}x + \varepsilon_{\nabla\Delta\phi L2}^{(i,k)} \end{aligned} \tag{14}$$

where $\nabla\Delta N_{L1}^{(i,k)}$ and $\nabla\Delta N_{L2}^{(i,k)}$ are fixed double-difference L1/L2 integer ambiguities.

An availability analysis is conducted to analyze the performance of the prescribed architecture. In this work, *availability* is defined as the percentage of time, per day, under which the fault-free vertical protection level (VPL_{H0}) is smaller than a vertical alert limit (VAL), assumed to be 1.1 m. VAL is an integrity requirement representing the tolerable error. VPL_{H0} is a function of the fault-free integrity risk (assumed to be 10^{-7}), the satellite geometry, and the precision of the GPS measurements. If the VPL_{H0} value exceeds the VAL, the system is said to be unavailable. VPL_{H0} is generated via a covariance analysis of the proposed SRGPS architecture. In this analysis, a maximum prefiltering period of 30 min is used to generate floating estimates of the wide-lane cycle ambiguities. When the UAV is close to the tanker, the broadcast floating wide-lane ambiguities from the tanker are combined with the UAV floating ambiguities. Geometric redundancy is exploited to fix those wide-lane and L1 and L2 integers that meet a 10^{-8} constraint for probability of incorrect fix. (In subsequent sensitivity analyses, described later in this paper, the fault-free integrity-risk requirement is relaxed to 10^{-4}, and the associated probability of incorrect fix is relaxed to 10^{-5}.) After the integer-fixing process, the position of the receiver aircraft can be estimated based on the visible satellites at the refueling point. The vertical component of the position-estimation standard deviation σ_v is calculated and used to generate the VPL_{H0} by multiplying σ_v by the integrity-risk multiplier corresponding to the integrity-risk requirement (5.33 in the case of 10^{-7} fault-free integrity risk).

Using different values of code and carrier sigmas (single-difference standard deviations), the service availability without blockage is calculated for an example Central Pacific location (22° N and 158° W) and is shown in Fig. 3. The single-difference sigmas $\sigma_{\Delta\mathrm{PR}}$ and $\sigma_{\Delta\phi}$ indicated in the figure are related to the raw sigmas σ_{PR} and σ_ϕ by a scaling factor of $\sqrt{2}$. These results (and those that follow) assume a first-order Gauss–Markov measurement error model with a time constant of 1 min to model multipath colored noise. In this

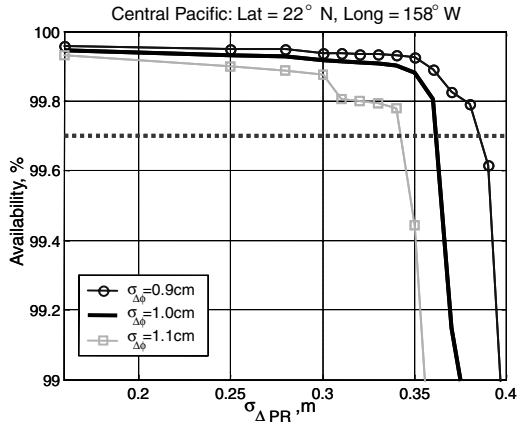

Fig. 3 Availability without sky blockage in the Central Pacific for different code and carrier sigma.

simulation, a 24-satellite [15] constellation is used. In addition, the effect of depleted GPS satellite constellations is also included, using the minimum standard constellation-state probability model provided in the GPS service performance standard (GPS SPS) [16]. These simulation parameters are used for all simulations conducted in this work, unless otherwise specified. Given the same requirements, AAR service availability is expected to be lower because of the shadowing caused by the tanker airplane. Therefore, before calculating the AAR availability, a satellite-blockage model must be established.

B. Availability Using a Simple Blockage Model

A preliminary blockage model is created by reverse-engineering masking geometries from photographs. Pictures of KC-135 tankers from different views are used to calculate the azimuth and elevation of the masking wedge that the tanker shadows from the sky (Fig. 4). The service availability is calculated based on the worst-case azimuth orientation of the tanker flight path at each sampled time during the day. [Vertical dilution of precision (VDOP) is used as the metric to define the worst case.] To determine the worst-case orientation for a given satellite geometry, it is not necessary to apply the azimuth-elevation mask to all possible orientations. Only the azimuths at which satellites are located need to be considered. Initially, the wedge is aligned with one of the satellites in view, and all of the satellites that fall in the masked region are eliminated from the constellation (Fig. 5). By rotating the wedge to be aligned with each of the satellites, the worst possible case (VDOP) is guaranteed to be captured. This method produces the same results as if all possible orientations are tested, but is more time-efficient.

For a KC-135, the masking-wedge size is approximately 65 deg in elevation and 100 deg in azimuth. A nominal 7.5-deg elevation mask is used outside the wedge. The corresponding availability results are shown in Fig. 6. Recall also that the preliminary AAR requirements and parameters detailed in Sec. II.A are used here. The results show

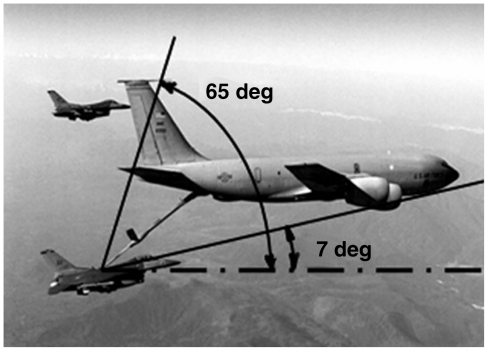

Fig. 4 Reverse engineering to determine the masking-wedge geometry of KC-135.

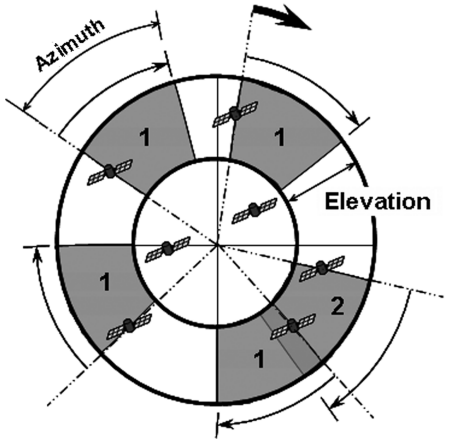

Fig. 5 Schematic diagram showing the method used to determine the worst VDOP (numbers indicate the number of blocked satellites for each iteration).

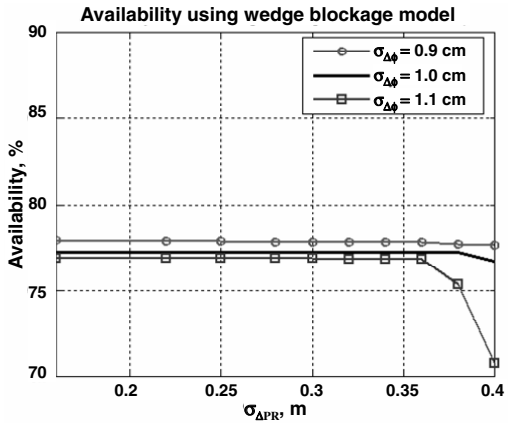

Fig. 6 AAR service availability in the Central Pacific using KC-135 wedge model.

that when the KC-135 blockage wedge mask is applied to the architecture, the availability drops from 99.9 to 77.2%. It is immediately clear that terminal navigation availability is highly sensitive to sky blockage. As discussed next, for other (smaller) tanker aircraft, the availability results would be somewhat better. Therefore, the sensitivity of availability to different wedge sizes (wedge azimuth and elevation values) is quantified.

For different tanker airplanes such as the KC-10 and KC-130, the same method of reverse engineering could not be used to determine the wedge angles, because of a lack of suitable images of these aircraft during refueling. Instead, a range of masks with different azimuth and elevation angles were used to span the different possible combinations of tankers, fighters, and refueling systems. The azimuth values used were 80, 100, 120, and 130 deg and the elevation angles were 35, 65, 75, and 85 deg Availability simulations were performed using all combinations of these wedge-angle values, $\sigma_{\Delta PR} = 30.0$ cm and $\sigma_{\Delta\phi} = 1.0$ cm. Figure 7 shows the availability at different wedge azimuth and elevation masks. It can be seen, for example, that the availability is reduced from 88 to 48% as the wedge azimuth increases from 80 to 130 deg, while holding the elevation mask at 65 deg. For the wedge sizes considered, the service availability ranges from 27 to 98%. Because of this extreme sensitivity to blockage, it is clear that a more accurate blockage model will be required to precisely define navigation availability. A detailed model for the KC-135 is described next.

C. Detailed Blockage Model

The previous results have shown that AAR terminal navigation availability is highly sensitive to the size of the sky blockage induced

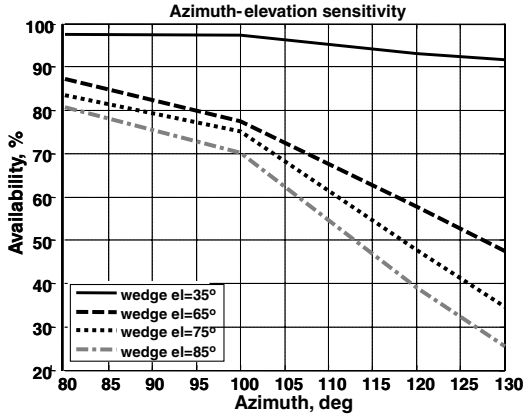

Fig. 7 Service availability in the Central Pacific as a function of wedge azimuth and elevation.

by the tanker. The wedge-blockage model used in the preceding initial analysis, although simple and efficient, is very conservative, because it covers areas in the sky that are not actually blocked by the tanker airplane. For this reason, a high-fidelity blockage model is developed using 3-D CAD drawings of the KC-135 obtained from The Boeing Company (Fig. 8).

The first step in generating the detailed blockage model is to convert the 3-D CAD drawing of the KC-135 tanker to a vertex matrix $\mathbf{M}$ containing coordinates of all n tanker vertices. This conversion can be done using commercial CAD programs. The vertex matrix is used as an input to the blockage model and needs to be reevaluated only when a different tanker aircraft is used. The geometry matrix $\mathbf{G}$ is prepared so that the refueling point (refueling boom tip) corresponds to the origin point [0, 0, 0]. This can be done by subtracting the value of the boom tip coordinate $\mathbf{b}$ from all of the rows of the vertex matrix $\mathbf{M}$:

$$\mathbf{G}_i = \mathbf{M}_i - \mathbf{b}^T, \qquad i = 1 \rightarrow n \tag{15}$$

where $\mathbf{b}$ is the boom tip coordinate vector (3×1); $\mathbf{G}_i$ is the ith row of the prepared geometry ($n \times 3$) matrix $\mathbf{G}$; $\mathbf{M}_i$ is the ith row of the raw vertex ($n \times 3$) matrix $\mathbf{M}$; and n is the number of vertices in the CAD model.

At this point, a C++ graphical library called OpenGL is used to extract a 2-D snapshot of the tanker in space. The OpenGL function library is frequently used by computer video game programmers to generate realistic 3-D games [17]. It is used here to convert the 3-D tanker model to a 2-D snapshot. This conversion is required to reduce the computation time and complications arising from verifying whether the satellite line-of-sight vector penetrates the 3-D tanker mesh. Therefore, a 2-D snapshot, which OpenGL efficiently provides, can be easily converted to azimuth and elevation angles using trigonometry. In short, OpenGL is analogous to a virtual photographic studio with a camera, different types of lenses, a projector, and a projector screen (on which the final 2-D snapshot will be presented). In AAR blockage, the camera is fixed at the origin point (boom tip) and oriented toward the tanker. The orientation of

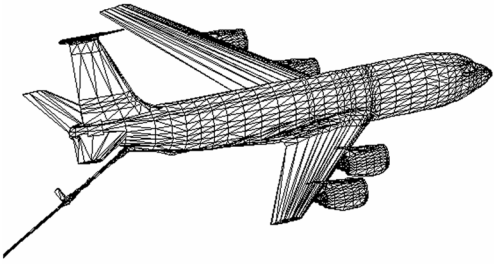

Fig. 8 CAD model used to generate the detailed blockage mask (courtesy of The Boeing Company).

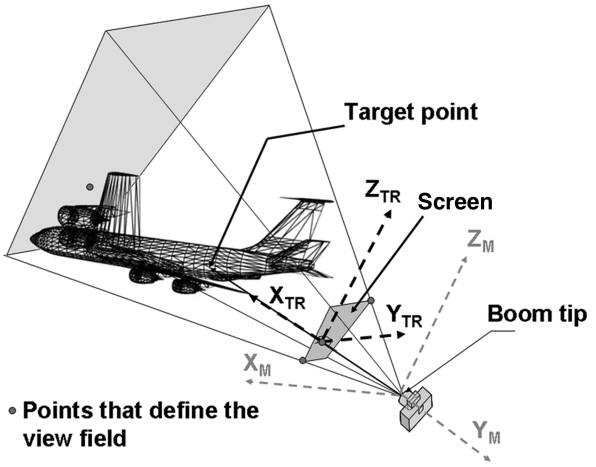

Fig. 9 Schematic diagram showing the model and the target frames.

the camera and the projection screen are defined by a line-of-sight vector between the camera and a specific target point in the tanker (Fig. 9). The target point is chosen based on trial-and-error experiments for different points and scenarios to ensure the best resolution performance. Euler angles of the target line-of-sight vector are used to define a new coordinate frame called the *target frame*. The lens is defined by the desired view field, which includes the view angle of the scene, and the nearest and farthest distances the camera can capture. To have the best resolution performance, the screen is located as far as possible from the camera. However, in OpenGL algorithms, the screen location also defines the nearest vision limit. Therefore, it must be placed between the camera and the target (the tanker) and as close as possible to the tanker (for resolution purposes). The screen parameters are calculated by transforming the geometry matrix $\mathbf{G}$ from the model frame M to the target frame TR, first using (3–2–1) rotation matrix ($^{\mathrm{TR}}\mathbf{R}^M$):

$$(\mathbf{G}^{\mathrm{TR}})^T = {}^{\mathrm{TR}}\mathbf{R}^M\mathbf{G}^M \tag{16}$$

where $\mathbf{G}^M$ is the geometry expressed matrix in the model frame ($n \times 3$); $\mathbf{G}^{\mathrm{TR}}$ is the geometry matrix expressed in the target frame ($n \times 3$); and $^{\mathrm{TR}}\mathbf{R}^M$ is the model-frame-to-target-frame rotation matrix (3×3).

The projection screen location is defined by the minimum value of the third column (Z direction) of the $\mathbf{G}^{\mathrm{TR}}$ matrix. The projections of the minimum and maximum values of the first and second column of the $\mathbf{G}^{\mathrm{TR}}$ matrix on the screen define the screen size (view angle) and the screen location in the X–Y plane. The furthest point the camera can capture is obtained by finding the maximum value of the third column of the $\mathbf{G}^{\mathrm{TR}}$ matrix. At this stage, the OpenGL function generates a 2-D pixel-based matrix representing the 2-D projection of the tanker on the screen. Because the real dimensions of the projection screen are already known (from the coordinates of the view field corners), the pixel-based matrix can be easily converted to a real dimension ($n \times n$) matrix in meters ($\mathbf{P}^{\mathrm{TR}}$). To calculate the azimuth and elevation angles of the imprinted shadow on the screen ($\mathbf{P}^{\mathrm{TR}}$), it is converted to the model frame using the following equation:

$$(\mathbf{P}^M)^T = {}^M\mathbf{R}^{\mathrm{TR}}\mathbf{P}^{\mathrm{TR}} \tag{17}$$

where $\mathbf{P}^M$ is the shadow matrix expressed in the model frame ($n \times 3$); $\mathbf{P}^{\mathrm{TR}}$ is the shadow matrix expressed in the target frame ($n \times 3$); and $^M\mathbf{R}^{\mathrm{TR}}$ is the target-frame-to-model-frame rotation matrix (3×3).

Using trigonometry, $\mathbf{P}^M$ can be converted to azimuth and elevation shadow vectors with respect to the boom tip [Eq. (18)]. The shadow matrix will be used to determine which satellites the tanker is blocking.

$$Az_i = \tan^{-1}\left(\frac{\mathbf{P}^M_{i,2}}{\mathbf{P}^M_{i,1}}\right) \qquad i = 1 \rightarrow n \tag{18}$$

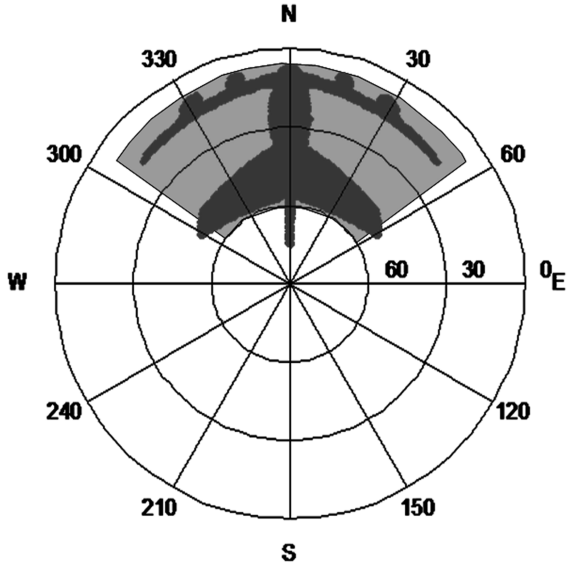

Fig. 10 Polar plot of the sky showing old and new blockage models.

$$El_i = \tan^{-1}\left(\frac{\mathbf{P}^M_{i,3}}{\sqrt{(\mathbf{P}^M_{i,1})^2 + (\mathbf{P}^M_{i,2})^2}}\right) \qquad i = 1 \rightarrow n$$

where Az_i is the azimuth angle corresponding to the ith pixel; El_i is the elevation angle corresponding to the ith pixel; and $\mathbf{P}^M_{i,k}$ is the (i, k) element of the shadow matrix in the model frame.

A sample plot that visually demonstrates the difference between the wedge-blockage model and the new blockage model is shown in Fig. 10. It is clear that the wedge-blockage model exaggerates the amount of the sky actually obstructed by the tanker.

D. Availability Sensitivity Analysis

Using the new blockage model, navigation availability sensitivity to other parameters, including elevation mask (outside the wedge), satellite constellation used, fault-free integrity-risk requirement, and use of the lateral alert limit (LAL) instead of VAL, is also quantified. In this analysis, the worst-case heading is chosen by finding the worst VDOP for 360 different heading cases (corresponding to 360–deg with a 1-deg increment). The results shown in Table 1 are for $\sigma_{\Delta PR} = 30$ cm and $\sigma_{\Delta\phi} = 1.0$ cm. The nominal case corresponds to the simulation parameters detailed in Sec. II.A and the wedge-blockage model in Sec. II.B. The benefit of using the detailed blockage model is made obvious by comparing the 77.5% availability using the wedge model to the 94.63% using the detailed model. In addition, because air refueling missions are conducted at high altitudes, the elevation mask outside the wedge can probably be safely lowered from 7.5 to 3 deg. The resulting availability is significantly improved from 94.63 to 99.48%. In contrast, relaxing the fault-free integrity-risk requirement from 10^{-7} to 10^{-4} (and also the cycle resolution probability of incorrect fix requirement from 10^{-8} to 10^{-5}) improves the availability by 1%. Finally, it is also shown in Table 1 that LAL availability is higher than VAL availability, but only by about 1% for LAL = 1.1 m. In summary, relaxing the fault-free integrity-risk requirement from 10^{-7} to 10^{-4} or using LAL instead of VAL (but keeping the level at 1.1 m) has little impact on the average service availability. However, using the 27-satellite constellation [18] (24 nominal and 3 operational spares) improves the availability to 97.65%. Based on the AAR program recommendations (for demonstration purposes), 3-deg elevation mask, 27-satellite constellation, and placement of the GPS antenna 60 in. aft of the nominal refueling boom tip have all been adopted as reasonable standard assumptions. Therefore, availability results for the combination of the three parameters are presented ($A + B + C$ in Table 1). The availability under this scenario is improved to 99.95%. These parameter values are also used to conduct the global availability analysis presented next.

Table 1 Navigation availability sensitivity to other parameters

Sensitivity parameter	Parameter value	Availability %
Nominal	NA	77.22
Blockage model	Detailed	94.41
Integrity risk	1×10^{-4}	95.16
LAL	1.1	95.59
Low-elevation mask, A	3 deg	99.40
Constellation, B	24 + 3 spare	97.65
Antenna location, C	60 in. aft boom tip	97.02
$A + B + C$	See the preceding parameters	99.95

III. Global Availability Simulations

A worldwide availability analysis is conducted using the described architecture and the detailed blockage model that was developed earlier. This phase of the study is designed to predict the visibility of GPS satellites using J-UCAS tanking aircraft (KC-135), and the resulting availability of a precise navigation solution is presented as a function of location on the globe and direction of flight. This latter variable is necessary because the shading of the tanking aircraft is not symmetrical with respect to the GPS satellite constellation, but depends on the direction of flight. The same requirements on VAL (1.1 m) [fault-free integrity risk (10^{-7}), $\sigma_{\Delta PR} = 30$ cm, and $\sigma_{\Delta\phi} = 1.0$ cm] and 30 min of prefiltering are used. As already noted, a 27-satellite constellation, an elevation mask of 3 deg, and an antenna located 60 in. aft the nominal refueling boom tip are used.

To study the effect of the geographic location of the airborne refueling mission on availability, a grid map of AAR locations is used (Fig. 11). The selected locations are distributed on a grid of 10° increments in longitude and latitude. In addition, to improve the resolution in the midlatitude regions, a finer grid size of 5° in latitude is implemented between latitudes of −40 and 40°. This simulation is executed for one sidereal day (23 h and 56 min) and for flight headings from 0 to 345 deg in 15-deg increments. In this study, due to computational burden considerations, the effect of a depleted constellation is not taken into account and availability is quantified by the number and length of observed navigation outages. Therefore, availability results are expected to be more optimistic than those presented in Table 1, because of the fault-free constellation assumption. A navigation outage is identified at the instant the VPL value becomes greater than the proposed 1.1-m VAL. Navigation outage maps are constructed for each flight heading and combined in a single composite plot in Fig. 12. In this map, we distinguish three levels of navigation outage durations: no navigation outage (clear areas), navigation outages of 1-min duration (wavy-pattern areas), and navigation outages greater than 1 min but less than 10 min (square-pattern areas). In addition, the *average availability* A_{avg} and *worst availability* A_{wrst} values are calculated using Eqs. (19) and (20), and the results with respect to the heading are shown in Table 2.

$$A_{\text{avg}} = \frac{m \cdot T - \sum_{i=1}^{m} T_{\text{out},i}}{m \cdot T} \tag{19}$$

$$A_{\text{wrst}} = \min_{i=1}^{m}\left(\frac{T - T_{\text{out},i}}{T}\right) \tag{20}$$

where A_{avg} is the average availability; A_{wrst} is the worst availability; m is the total number of grid points; T is the number of minutes per sidereal day (1436); and $T_{\text{out},i}$ is the total outage duration for grid point i.

One-minute outages are not accounted for in T_{out}, because it was assumed that an integrated INS system would be capable of bridging outages of up to 1 min in duration. Figure 12 shows that there is not a

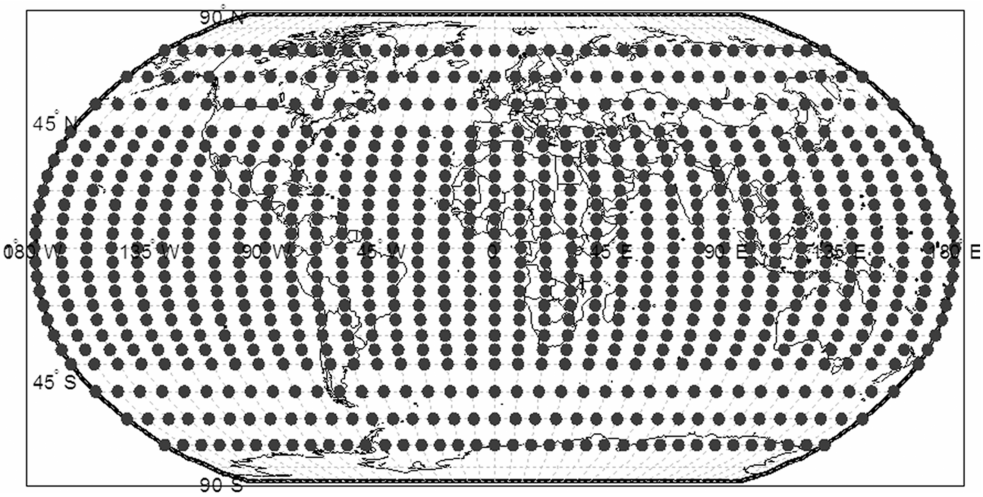

Fig. 11 World map showing the simulation grid points.

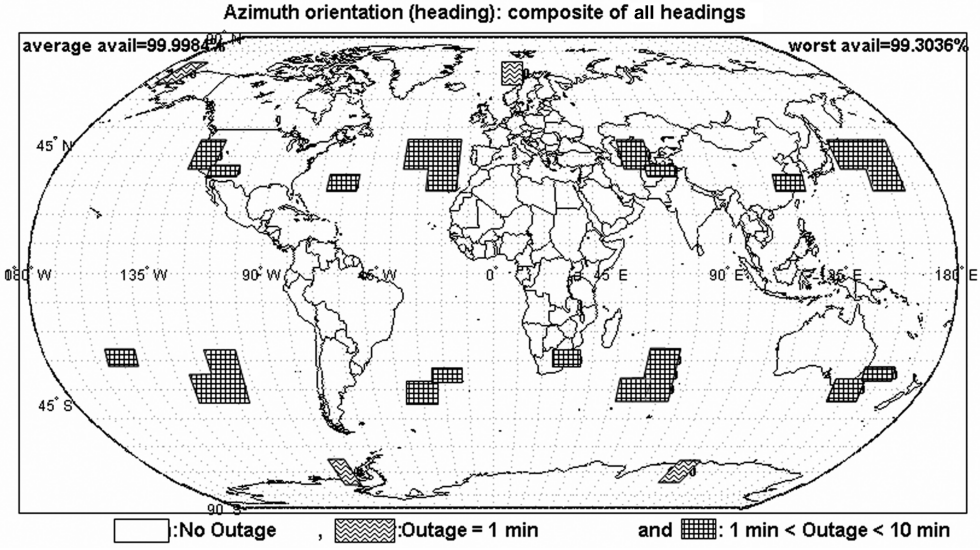

Fig. 12 Composite map of all headings showing the outages at the grid points.

single incident of an outage lasting more than 10 min for any grid point with any heading. The worst availability for any grid point and composite heading is 99.30%. However, the average availability over all headings and all grid points is 99.9985%. These results and the results shown in Table 2 are encouraging because they show that there is always a time/heading combination that allows the UAV to be refueled autonomously all over the globe.

Table 2 Global availability results (average and worst availability) for different heading angles

Heading, deg	A_{avg}, %	A_{wrst}, %
0	99.9990	99.8607
30	99.9990	99.8607
90	99.9948	99.6518
150	99.9990	99.8607
180	99.9990	99.8607
255	99.9876	99.4429
270	99.9959	99.8607
285	99.9876	99.4429
All other headings	100	100
Composite	99.9984	99.3036

IV. Blockage-Model Validation

To initially validate the detailed blockage-model process, a three-vertex geometry is used as a benchmark test. The azimuth and elevation angles of the three vertices are easily calculated analytically and compared with the model-generated results. Then the complete set of tanker vertices are used to compare 3-D CAD views from the boom tip to the corresponding OpenGL shadow snapshots. (These tests are implemented in MATLAB®, using a camera located at the boom tip and aimed at the target point on the tanker.) The results consistently exhibit precise matches. An example result is shown in Fig. 13. At this point, the blockage model is ready to be tested in a flight test environment.

A. AAR Flight Test

As mentioned earlier, when the UAV enters the service volume, it performs a covariance analysis based on the predicted visible satellites at the contact position. The blockage model predicts which satellites will be masked by the tanker. Based on the predictive simulation results, the algorithm makes the decision to continue or abort the mission and provide an alternative heading. Therefore, the main goal of this section is to validate the blockage model and quantify its performance in real flight conditions. Validation of the

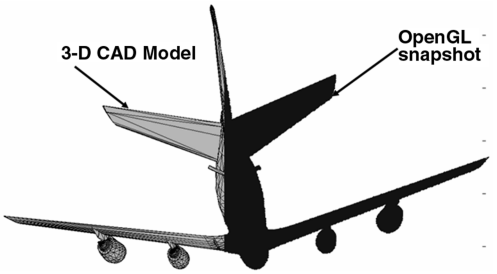

Fig. 13 Matching the 3-D CAD drawing as seen from the Lear antenna with the OpenGL snapshot.

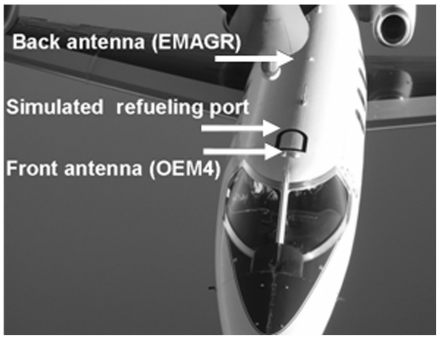

Fig. 14 Antenna locations on the Lear jet airplane.

navigation algorithms and integrity will be provided in future flight tests.

AAR flight tests were conducted in September 2004 to collect time-tagged GPS and INS data that were postprocessed to validate the sky-blockage model. In these tests, a Lear jet was used as a surrogate for the UAV. The algorithms developed in this work were not used to navigate the Lear tanker formation. Instead, the Lear pilot regulated his aircraft's position relative to the tanker boom (which was lowered during the flight test, but without being engaged) visually and based on commands received from the boom operator inside the tanker. The Lear jet was equipped with two GPS antennas: a front antenna that was connected to a NovAtel OEM4 receiver and a back antenna that was connected to a Rockwell EMAGR receiver (Fig. 14). The tanker had only one GPS antenna, which was connected to both OEM3 and EMAGR receivers. To help in planning the flight test, simulations were performed to define the flight times and azimuths that minimize GPS availability (i.e., maximize blockage). The flight test took place in the Niagara Falls area (43° N and 97° W) during the second and third weeks of September 2004. In these simulations, GPS almanac data from 22 July 2004 were used to provide predictions for a test date of 15 September 2004. The mission planning results were also applicable for other days during the flight test window by simply shifting outage events by 4 min per day. In these simulations, $\sigma_{\Delta PR} = 30$ cm and $\sigma_{\Delta\phi} = 1.0$ cm were assumed.

Nineteen different test point positions for the boom were used in the flight test to cover the KC-135 in-flight refueling envelope (Fig. 15). In the mission planning process, these specified boom positions were used to generate a series of sky-blockage matrices (one for each boom position). Using the sky-blockage matrices, simulations for each of the boom points were conducted and the quantitative time trace results for VPL values, satellites in view, and sky blockage were recorded. The resulting database was used to plan the Lear tanker's formation-flight-test paths (straight path relative to the ground) by flying in the direction (heading) and time slot for each test point when the satellite blockage or the satellite geometry is the worst. Samples of the plots that are used in preparing the flight test cards are shown in Figs. 16 and 17.

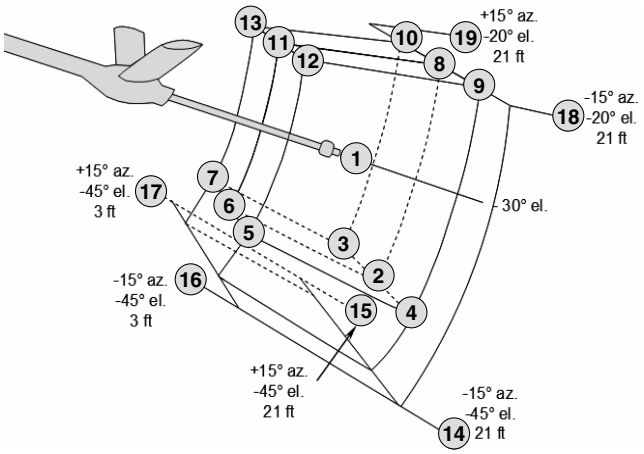

Fig. 15 Different test points that define the refueling envelope of the KC-135.

The data collected from the flight test was postprocessed to validate the blockage model. The tanker aircraft usually flies in a racetrack pattern that is limited by the refueling airspace. The racetrack pattern consists of two straight legs and two turn legs, as shown in Fig. 17. The KC-135 is capable of providing 1000 gal/min of fuel through its boom. If the straight leg is long enough to refuel the UAV aircraft, a straight and level refueling mission is conducted. However, if the airspace is small and the refueling time exceeds the straight-leg time, a racetrack refueling mission (in which the UAV is in contact position and the boom is engaged through the turn legs)

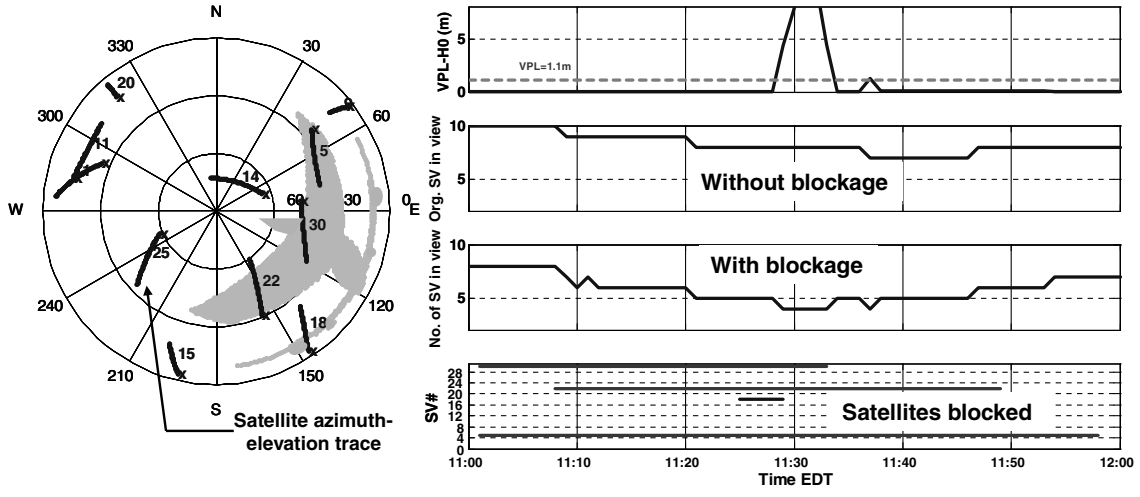

Fig. 16 Samples of the flight test simulation results used in preparing the flight test cards (SV is the satellite vehicle).

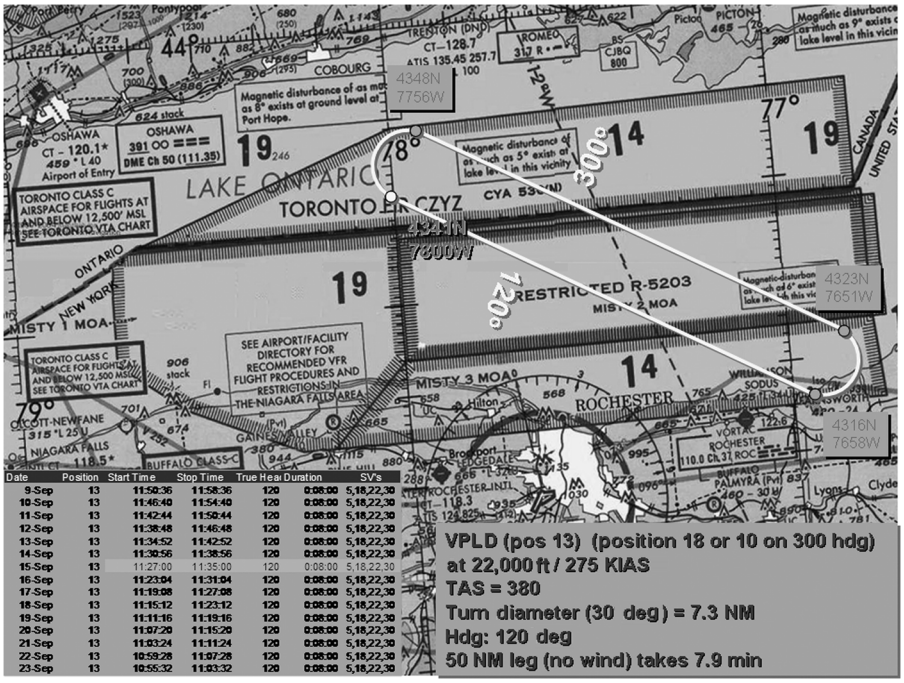

Fig. 17 Samples of the flight test cards provided in the mission.

becomes necessary. In this work, it is assumed that the straight-leg time is enough to refuel the UAV. Therefore, all simulations are based on straight and level refueling only. (Modeling racetrack simulations will be considered in future work.) Because the total flight test duration was approximately 50 min, many racetrack refueling patterns were performed. Although the individual racetracks mimic the actual refueling racetrack, it is quite uncommon for the receiving aircraft (the Lear in this case) to have multiple racetracks in an actual refueling mission.

In previous blockage simulations, the relative vector and the attitude of both aircraft were assumed to be static during refueling. However, to analyze the actual flight data, the fact that both aircraft are moving continuously must be considered. Therefore, a new model, which accounts for the dynamic changes, is constructed (Fig. 18). The dynamic model uses the tanker attitude and relative position vector to place the tanker with respect to the Lear antenna instead of using the boom tip (as in simulations). The relative position vector is estimated through a prototype AAR relative navigation algorithm that was developed earlier [19]. Because the Lear performed many racetracks while being in the contact position, many satellite outages and phase-lock losses were observed in the recorded data. Although these outages will not impact the blockage-model validation directly, they may degrade the certainty in the relative vector estimation. More details about the vector estimation can be found in [19]. The Lear attitude does not affect the shadow masking; instead, it only changes the low-elevation mask for its antenna. In addition, the attitude information from the tanker is used to orient the tanker in space using the attitude-corresponding rotation matrices.

The refueling boom is also captured in this model. Because real-time boom extension and orientation parameters are not available in the test data, the boom is assumed to be always pointed toward the front Lear GPS antenna (referred to as OEM4). This is done by extracting the boom elements from the CAD model and then aligning the boom with the (time-varying) line segment between OEM4 and the pivot boom point on the tanker. This approximation is chosen

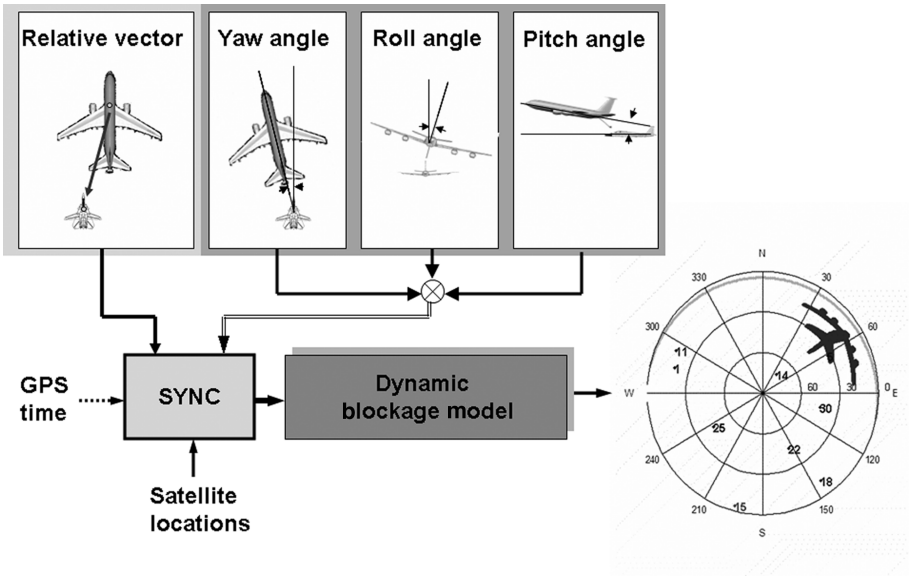

Fig. 18 Three-dimensional dynamic blockage-model algorithm structure.

based on Fig. 14, in which it can be seen that the simulated refueling point is very near the OEM4 antenna. The tanker masking shadow and the blocked satellites are then found using the same algorithm described earlier. This process is done at each epoch (2-s intervals) during host flight data analysis.

B. Blockage-Model Validation Using Flight Test Data

The collected GPS and INS data from both the airplane and the relative position vector history generated in earlier work [19] are used in blockage-model validation. The data set that is used in the validation corresponds to data recorded on 21 September 2004 from 1100:38 to 1108:48 hrs. This time is specifically selected because it includes flying at the heading of maximum blockage, shown in Fig. 16. When comparing the blocked satellites predicted by the model with the measurement outages, it was found that the blockage model is conservative in the sense that there are points at which satellites are predicted to be blocked by the model, but phase lock is not actually lost. To determine if the discrepancies are due to a defect in the blockage model, carrier-to-noise ratio (C/N0) values for those satellites that are predicted to be blocked are examined.

The black dots in Fig. 19 represent the measured C/N0 values corresponding to the L1 signal for satellite 30 (PRN30). A C/N0 value of zero means that the satellite is not visible (totally blocked). The shaded area represents the blockage-model prediction for PRN30. As mentioned earlier, it can be seen that the blockage model does not always match the satellite outages. In the case of clear sky (the first 100 s), C/N0 values are around 48 dBHz. Once PRN30 is predicted to be blocked by the blockage model, a drop in C/N0 is noticed. By comparing the times when PRN30 is predicted to be blocked with the times when C/N0 values degrade, it is clear that they generally concur. An exception would be the last few points at the end of the shaded area, for which the blockage model predicts the satellite to be in clear sky, although no measurement is received. This can be explained by the fact that PRN30 has been blocked for a long time and so time will be needed for the GPS receiver to reacquire it. In other words, the blockage model did not fail in identifying PRN30 as being blocked by the tanker. In addition, signal-power degradation is evidence that the signal could penetrate certain parts of the tanker.

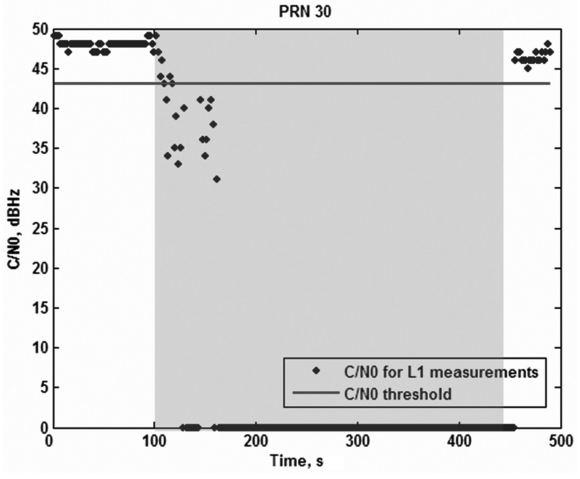

Fig. 19 Measured carrier-to-noise ratio (C/N0) for PRN-30 (shaded area represents the blockage prediction).

To quantify the power loss caused by the blockage in a consistent and general way that can be used in validating the accuracy of the blockage model, a C/N0 threshold is used. As an example, in Fig. 19, a threshold of 43 dBHz is considered reasonable. To generalize the threshold selection criteria, a nominal C/N0 threshold value is, with much attention, chosen to be 5 dBHz less than the average of the previously observed obstruction-free C/N0 values, to identify signal blockage. Choosing a threshold that can be used for all satellites is a tradeoff process. If the threshold is too tight, the natural variation in C/N0 might appear as blockages. In contrast, if the threshold is too loose, it might not capture instances when the satellite signal penetrates the tanker.

Figure 20 is constructed to compare the blockage-model prediction with the signal quality for the satellites that encounter blockages. In Fig. 20, the gray circles represent the blockage-model prediction and the solid dots indicate a measured C/N0 value below the threshold. In addition, the shaded area in the plot represents periods in which the standard deviation of the positioning solution is poor (standard deviation greater than 26 cm [19]). By comparing occurrences of target satellites predicted to be blocked (in circles) with occurrences of C/N0 values falling below the threshold, it was found that the events generally coincide, especially when the relative position error standard deviation is relatively good (less than 3 cm [19]). The correspondence of the blockage model and C/N0 drops shown in Fig. 20 is quantified in Table 3.

In Table 3, two different quantification metrics are introduced: *missed measured outage* and *missed predicted outage*. Missed measured outage represents the percentage of points that are predicted to be clear out of the measured blocked points (C/N0 is below the threshold). Missed predicted outage, on the other hand, is defined as the percentage of points that are measured as clear (C/N0 is greater than the threshold) out of the predicted-blocked points. Therefore, if both percentages are zero, then the blockage

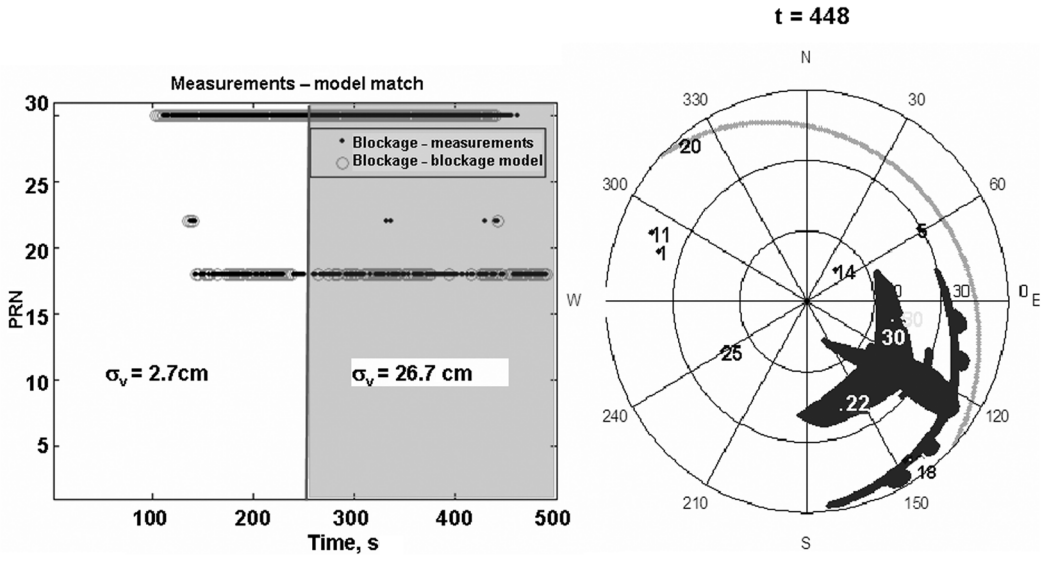

Fig. 20 Comparison between the blockage-model prediction and the signal quality for the satellites that encounter blockages.

Table 3 Quantitative results showing the blockage-model performance shown in Figure 20

PRN	Elevation, deg	Measured blocked (points)	Missed measured outage, %	Predicted to be blocked (points)	Missed predicted outage, %
18	12	135	36.3	111	22.5
22	40	8	62.5	4	25.0
30	45	173	5.2	169	3.0

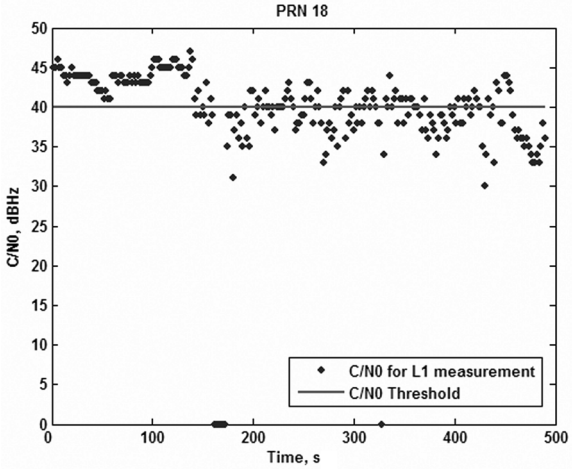

Fig. 21 Measured carrier-to-noise ratio (C/N0) for PRN-18.

performance is perfect. In addition, to provide a stochastic basis for these percentages, the number of points that are measured as blocked and predicted to be blocked are shown in Table 3. As a result, Table 3 reveals that the blockage-model performance is good with respect to satellite 30 (PRN30). In the case of PRN22, the number of comparison points is very low, and so statistically there is little that can be inferred about the blockage model. In addition, Fig. 20 shows that the mismatch cases for PRN22 happen when the relative position error standard deviation is poor. In the other case, PRN18 is a low-elevation satellite (12 deg). Therefore, the mismatching can be caused by the definition of the signal blockage. As mentioned earlier, a blockage is defined when C/N0 drops below the average by a 5-dBHz threshold. Such a threshold might be inappropriate for low-elevation satellites, because there is a greater degree of natural variation in C/N0 at low elevations, as shown in Fig. 21.

Similar analyses were conducted on two other sets of flight test data recorded on 21 September 2004 from 1404:08 to 1414:48 hrs and 22 September 2004 from 1246:28 to 1251:28 hrs. The quantitative results for these two days are shown in Tables 4 and 5, respectively. As was the case with the earlier data set, the results reveal that the blockage-model performance is good with respect to high-elevation satellites (PRN25 in Table 4 and PRN9 in Table 5). However, as discussed earlier, lower-elevation angles do not exhibit the same performance, because the C/N0 metric used to define signal blockage is also sensitive to the weaker antenna gain at low elevations. The only additional exception is PRN18 in Table 5. Although PRN18 is a high-elevation satellite, the missed-measured-outage percentage is high. However, after further inspection, it was found that PRN18 was totally blocked (no signal could be tracked at the GPS receiver) for 50 s. Later, when PRN18 came into the clear sky, the GPS receiver needed time to reacquire it. As a result, the data show PRN18 as "measured blocked," although the blockage model predicted the satellite to be in clear sky.

The measured C/N0 and phase-lock loss usually concur with the blockage-model prediction. This correspondence provides strong evidence toward the validation of the dynamic blockage model. Remaining occurrences of data–model discrepancy do exist for some satellites. Two probable interpretations have been suggested for these occurrences: one is that the signal gets weaker when penetrating the tanker body, but stays strong enough to maintain signal lock and remain above the defined threshold (predicted to be blocked and measured as clear), the other is that the signal gets diffracted by the edges of the wings and stabilizers or reflected (multipath), and the value of C/N0 falls below the threshold (predicted to be clear and measured as blocked). The blockage model developed in this work is conservative in that it assumes that any signal that penetrates the tanker body is blocked. This assumption is necessary due to lack of knowledge of the signal noise characteristics after penetrating different parts of the tanker. In addition, if the system availability is demonstrated to be acceptable using the conservative assumption, any further model that takes the signal power and noise into account will only serve to improve the performance of the navigation system. In future work, a static KC-135 ground test is recommended to assess the magnitude of the assumed signal penetration, multipath degradation, and noise characteristics of the penetrative signals.

V. Conclusions

A carrier-phase differential GPS algorithm was used to evaluate terminal navigation performance for AAR. To make this algorithm

Table 4 Quantitative results showing the blockage-model performance for 21 September 2004 1421–1429 hrs data

PRN	Elevation, deg	Measured blocked (points)	Missed measured outage, %	Predicted to be blocked (points)	Missed predicted outage, %
6	21	190	13.5	243	32.5
25	56	297	5.1	282	0.0

Table 5 Quantitative results showing the blockage-model performance for 22 September 2004 0858–0908 hrs data

PRN	Elevation, deg	Measured blocked (points)	Missed measured outage, %	Predicted to be blocked (points)	Missed predicted outage, %
5	16	45	53.3	27	22.2
9	52	28	10.7	25	4.0
18	67	59	54.2	30	10.0
21	25	51	58.8	27	22.2

applicable to AAR, sky-blockage models were developed and were used to study the sensitivity of navigation availability to required fault-free integrity risk, elevation mask, and constellation. In addition, a worldwide global analysis for GPS positioning was conducted and the results were presented. GPS positioning performance for the AAR application is promising in the sense that the average availability is 99.9985% and the worst availability is 99.3036% for all headings and geographic locations examined. AAR flight tests were conducted to validate the blockage model. Simulations of AAR flight test missions that took place in September 2004 were performed and the results were used in the planning of these missions. The blockage model was validated using benchmark tests and postprocessing of the flight test data. The remaining discrepancies could not be directly attributed to the blockage model, but may be related to signal penetration or degradation caused by multipath reflection or diffraction on the tanker.

Acknowledgments

The authors gratefully acknowledge the Naval Air Warfare Center Aircraft Division (NAWCAD) for supporting this research. The authors would like to specifically acknowledge the support and guidance of Glenn Colby (NAWCAD) and the constructive comments and suggestions that were provided by Mathieu Joerger (Illinois Institute of Technology) regarding this work.

References

[1] Stephenson, J. L., "The Air Refueling Receiver That Does Not Complain," Master's Thesis, School of Advanced Airpower Studies, Maxwell AFB, AL, Oct. 1999.

[2] Hebert, A., "New Horizons for Combat UAVs," *Air Force Magazine*, Vol. 86, No. 12, Dec. 2003, pp. 70–73.

[3] Kramlinger, G. D., "Narrowing the Global-Strike Gap with an Airborne Aircraft Carrier," *Air & Space Power Journal*, Vol. 19, No. 2, 2005, pp. 85–98.

[4] Pollini, L., Campa, G., Giulietti, F., and Innocenti, M., "Virtual Simulation Setup for UAVs Aerial Refueling," AIAA Modeling and Simulation Technologies Conference, Austin, TX, AIAA Paper 2003-5682, Aug. 2003.

[5] Kimmett, J., Valasek, J., and Junkins, J. L., "Autonomous Aerial Refueling Utilizing a Vision Based Navigation System," Proceedings of AIAA Guidance, Navigation, and Control Conference, Monterey, CA, AIAA Paper 2002-4469, Aug. 2002.

[6] Tandale, M., Bowers, R., and Valasek, J., "A Robust Trajectory Tracking Controller for Vision Based Autonomous Aerial Refueling of Unmanned Aircraft," Proceedings of AIAA Guidance, Navigation, and Control Conference, San Francisco, CA, AIAA Paper 2005-5868, Aug. 2005.

[7] Misra, P., and Enge, P., *Global Positioning System Signals, Measurements, and Performance*, Ganga–Jamuna, Lincoln, MA, 2001, Chaps. 4–7.

[8] Cohen, C. E., Pervan, B. S., Lawrence, D. G., Cobb, H. S., Powell, J. D., and Parkinson, B. W., "Real-Time Flight Test Evaluation of the GPS Marker Beacon Concept for Category 3 Kinematic GPS Precision Landing," *ION GPS-93* [CD-ROM], Inst. of Navigation, Fairfax, VA, 1993.

[9] Lachapelle, G., Sun, H., Cannon, M. E., and Lu, G., "Precise Aircraft-to-Aircraft Positioning Using a Multiple Receiver Configuration," *Institute of Navigation National Technical Meeting 1994*, Inst. of Navigation, Fairfax, VA, 1994, pp. 793–799.

[10] Heo, M., Pervan, B., Pullen, S., Gautier, J., Enge, P., and Gebre-Egziabher, D., "Robust Airborne Navigation Algorithm for SRGPS," *PLANS2004: Position, Location, and Navigation Symposium*, Inst. of Electrical and Electronics Engineers 2004, pp. 175–183.

[11] Dogra, S., Wright, J., and Hansen, J., "Sea-Based JPALS Relative Navigation Algorithm Development," *ION GNSS 2005* [CD-ROM], Inst. of Navigation, Alexandria, VA, 2005.

[12] McGraw, G. A., Young, R. S. Y., "Dual Frequency Smoothing DGPS Performance Evaluation Studies," *Institute of Navigation National Technical Meeting 2005* [CD-ROM], Inst. of Navigation, Fairfax, VA, 2005.

[13] Teunissen, P., Odijk, D., and Joosten, P., "A Probabilistic Evaluation of Correct GPS Ambiguity Resolution," *ION GPS-98* [CD-ROM], Inst. of Navigation, Alexandria, VA, 1998.

[14] Teunissen, P., "GNSS Ambiguity Bootstrapping: Theory and Application," *Proceedings of KIS2001*, Dept. of Geomatics Engineering, Univ. of Calgary, Calgary, Alberta, Canada, 2001, pp. 246–254.

[15] "Minimum Operational Performance Standards for Global Positioning System/Wide Area Augmentation System Airborne Equipment," Radio Technical Commission for Aeronautics (RTCA, Inc.), Rept. DO-229C, Washington, D.C., Nov. 2001, Appendix B.5.

[16] "Global Positioning System Standard Positioning Service Performance Standard," Oct. 2001.

[17] Neider, J., Davis, T., *OpenGL Programming Guide: The Official Guide to Learning OpenGL, Ver. 1.1*, Addison Wesley Longman, Reading, MA, 1997, Chaps. 1–4.

[18] Massatt, P., Fritzen, F., and Perz, M., "Assessment of the Proposed GPS 27-Satellite Constellation," *ION GPS/GNSS 2003* [CD-ROM], Inst. of Navigation, Alexandria, VA, 2003.

[19] Khanafseh, S., Pervan, B., Gautier, J., Enge, P., and Colby, G., "Validation of Autonomous Airborne Refueling Algorithms Using Flight Test Data," *ION GNSS 2005* [CD-ROM], Inst. of Navigation, Fairfax, VA, 2005